

# Performance Evaluation of the Ionospheric Threat Mitigation Strategies in Dual-Frequency Multi-Constellation GBAS

Maria Caamano

*Institute of Communications and Navigation  
German Aerospace Center (DLR)  
Wessling, Germany  
maria.caamanoalbuerno@dlr.de*

Daniel Gerbeth

*Institute of Communications and Navigation  
German Aerospace Center (DLR)  
Wessling, Germany  
daniel.gerbeth@dlr.de*

Hiroatsu Sato

*Institute for Solar-Terrestrial Physics  
German Aerospace Center (DLR)  
Neustrelitz, Germany  
hiroatsu.sato@dlr.de*

Mihaela-Simona Circiu

*Directorate of Tech., Eng. and Quality  
European Space Agency (ESA)  
Noordwijk, The Netherlands  
simona.circiu@esa.int*

Michael Felux

*Centre for Aviation, School of Engineering  
Zurich University of Applied Sciences (ZHAW)  
Winterthur, Switzerland  
felu@zhaw.ch*

**Abstract**—In this paper, we evaluate the performance of the dual-frequency airborne ionospheric gradient monitor proposed for dual-frequency multi-constellation (DFMC) Ground Based Augmentation Systems (GBAS) at different distances from the airport. We use two types of thresholds for this assessment: (i) a constant threshold derived from operational requirements, and (ii) a dynamic threshold that increases with the distance from the airport. Increasing the threshold allows more ionospheric error within the position solution, but also enables the use of the primary single-frequency modes without the need to switch to the ionosphere-free (Ifree) solution for a longer period, which generally degrades the performance because it combines the noise and multipath of two frequencies. Furthermore, we compare the performance of the two potential architectures for DFMC GBAS: (i) the so-called GAST F architecture, which is based on single-frequency 100 seconds smoothing, and (ii) the GAST X architecture, which is based on divergence-free (Dfree) smoothing with variable and potentially longer smoothing time constants. Results with both simulated and real data show that the use of a variable threshold significantly reduces the probability of excluding satellites and switching to the Ifree mode for both GAST F and X, thereby increasing the availability of GBAS.

**Index Terms**—Dual-frequency multi-constellation GBAS, ionospheric monitoring, availability, integrity, anomalous ionospheric gradients

## I. INTRODUCTION

The Ground Based Augmentation System (GBAS) is a local-area, airport-based augmentation of Global Navigation Satellite Systems (GNSS) that provides precision approach guidance for aircraft. GBAS enhances GNSS performance in terms of integrity, continuity, accuracy, and availability by providing differential corrections and integrity information to aircraft users. Differential corrections, which are provided only for the L1 signals of GPS in current operational GBAS, enable the aircraft to remove most of the spatially correlated errors between the ground station and the aircraft. Additionally,

integrity parameters enable the airborne system to calculate bounds of the residual position errors and ensure the safety of the operation. However, abnormally large ionospheric gradients acting between the GBAS station and the aircraft on approach present a threat to users since the position errors caused by these gradients are not corrected through the application of the corrections [1]. Thus, it is essential to monitor and exclude affected satellites to guarantee system integrity and safety. Several mitigation strategies are implemented in current systems [2]–[4], but they lead to a degradation of availability in areas with active ionosphere [3], [5].

With the introduction of a second frequency (L5/E5a) usable for civil aviation and the development of additional constellations (e.g. Galileo), new GBAS architectures and monitoring capabilities are emerging and can be exploited. One of the new GBAS architecture candidates, developed primarily in the Single European Sky ATM Research (SESAR) program in Europe, proposes to send mainly pseudorange corrections and integrity parameters to the aircraft and uses 100-second smoothed pseudoranges on the L1/E1 frequency to compute the position of the aircraft. This first architecture is known as the GBAS Approach Service Type F (GAST F) [6]. Another option, known as GAST X and being developed primarily in the United States, proposes to send the raw measurements to the aircraft and uses divergence-free (Dfree) positioning with a longer smoothing time constant [7]. The main similarities between both architectures are [8]:

- Both architectures have a primary mode that uses L1/E1 carrier-smoothed code measurements.
- Both architectures implement an airborne ionospheric gradient monitor based on dual frequency (L1/E1 and L5/E5a frequencies) to mitigate the anomalous iono-

spheric gradient threat ([9], [10]).

- Both architectures will fall back to an ionospheric-free (Ifree) position solution when the performance on the primary modes is not sufficient. Forming an Ifree combination of the dual-frequency measurements to compute the position removes the first order ionospheric error. However, in this case the noise and multipath of both frequencies is combined, leading to a degraded nominal performance of the navigation solution. Therefore, a switch to the Ifree mode is triggered only when the performance of the primary modes is not sufficient due to extremely high ionospheric activity.

The main differences between both architectures are:

- GAST F uses single-frequency (SF) L1/E1 smoothing with a fixed smoothing time of 100 seconds whereas GAST X uses divergence-free (Dfree) smoothing with varying smoothing times up to 600 seconds. Therefore, it is expected that GAST X has lower residual errors due to: (i) lower levels of noise and multipath thanks to the longer smoothing, and (ii) the removal of the single-frequency filter build up errors thanks to the Dfree smoothing.
- The calculation of the test statistic for the airborne ionospheric gradient monitor is slightly different in GAST F and GAST X (see Sections III-A and III-C) ([9], [10]).
- In GAST F, the airborne ionospheric gradient monitor excludes satellites with large errors, which allows to find a subset of satellites with sufficient performance to continue the operation on the primary mode [9]. In contrast, the GAST X version of the monitor triggers a switch to the Ifree mode directly if a constant threshold of 7 meters is exceeded ([8], [11]).
- GAST X processing at the aircraft receiver is more complex than GAST F.
- As the capacity of the Very High Frequency Data Broadcast (VDB) link is limited, GAST X might be able to transmit information for less satellites than GAST F. However, in this paper, we assume that both architectures have the same number of satellites available.

In previous work, we proposed a dual-frequency airborne ionospheric monitoring scheme to support the so-called GAST F architecture [9]. We designed a combined test statistic for multiple affected satellites simultaneously and proposed a threshold derived from operational requirements. This threshold, an adaptation of the one proposed in [12], is only dependent on the glidepath angle transmitted by the ground station and the performance of the autopilot and navigation system installed at the aircraft. However, it has only been validated with very limited simulated data [9], and with real data in nominal conditions from static user receivers located very close to the GBAS reference point.

In this paper, we propose a new threshold for the dual-frequency airborne ionospheric gradient monitor that increases with the distance from the airport, similar to the Alert Limits (ALs) as described in the next sections. Furthermore, we evaluate the performance of the monitor for the two potential

architectures being considered for future DFMC GBAS (i.e. GAST F and GAST X) with both simulated and real data.

## II. BACKGROUND ON PROTECTION LEVEL CALCULATION

First, we give a short overview about the computation of Protection Levels (PLs), which we use in the following sections to assess the performance of each processing mode and architecture (i.e., GAST F or GAST X). These protection levels are defined as position error bounds at the defined integrity risk probabilities ( $2.0 \cdot 10^{-7}$  per approach) [13]. They address the fault-free condition (H0), the case of a failure in one of the reference receivers (H1), and the position errors due to errors in the ephemeris data. The aircraft computes the maximum among the three and verifies if the values are below the lateral and vertical alert limits (LAL and VAL respectively). In case the protection levels exceed the alert limits, GBAS is set to unavailable. As the Vertical Protection Level (VPL) is usually larger than the Lateral Protection Level (LPL) while the VAL is smaller than the LAL, our assessments are based on the VPL and the VAL. The vertical protection level in fault-free conditions ( $VPL_{H0}$ ) is calculated at each epoch using Equation 1 [14]:

$$VPL_{H0} = k_{ffmd} \cdot \sqrt{\sum_{i=1}^N s_{vert,i}^2 \cdot \sigma_{GBAS,i}^2}, \quad (1)$$

where index  $i$  indicates the  $i$ -th satellite of the  $N$  satellites used for the VPL computation and  $\sigma_{GBAS,i}^2$  is the variance of a normal distribution that bounds the true post-correction range-domain error distribution for satellite  $i$  under the fault-free hypothesis. The fault-free missed detection multiplier  $k_{ffmd}$  is set to 5.81 according to [14], fulfilling the above mentioned integrity constraints for a base station with three reference receivers. The components of  $\sigma_{GBAS,i}^2$  are:

$$\sigma_{GBAS,i}^2 = \sigma_{gnd,i}^2 + \sigma_{tropo,i}^2 + \sigma_{air,i}^2 + \sigma_{iono,i}^2, \quad (2)$$

where  $\sigma_{gnd,i}$  is the total fault-free standard deviation of the error included in the differential corrections for satellite  $i$ ,  $\sigma_{tropo,i}$  is the standard deviation of the error term associated with residual tropospheric uncertainty for satellite  $i$ ,  $\sigma_{air,i}$  the corresponding error term that bounds fault-free airborne receiver multipath and noise errors for satellite  $i$ , and  $\sigma_{iono,i}$  accounts for the nominal residual ionospheric uncertainty for satellite  $i$ . The  $s_{vert,i}$  are calculated as follows:

$$s_{vert,i} = s_{3,i} + \tan(\theta_{GPA}) \cdot s_{1,i}, \quad (3)$$

where  $\theta_{GPA}$  is the glidepath angle (typically  $3^\circ$ ) and  $s_{1,i}$  and  $s_{3,i}$  correspond to the first and the third rows of the pseudoinverse  $\mathbf{S}$  of the weighted geometry matrix  $\mathbf{G}$  containing all the available satellites, which can be written as:

$$\mathbf{S} = (\mathbf{G}^T \mathbf{W} \mathbf{G})^{-1} \mathbf{G}^T \mathbf{W}. \quad (4)$$

Each row  $g_i$  of  $\mathbf{G}$  is defined as:

$$[-\cos(el_i) \cdot \cos(az_i) \quad -\cos(el_i) \cdot \sin(az_i) \quad -\sin(el_i) \quad 1], \quad (5)$$

with  $el_i$  and  $az_i$  being the elevation and azimuth of the  $i$ -th satellite respectively. The inverse of the weighting matrix is defined as:

$$\mathbf{W}^{-1} = \begin{pmatrix} \sigma_{GBAS,i}^2 & \cdots & 0 \\ \vdots & \ddots & \vdots \\ 0 & \cdots & \sigma_{GBAS,N}^2 \end{pmatrix}, \quad (6)$$

where  $\sigma_{GBAS,i}^2$  are the ones calculated in Equation 2. Note that, in the case where measurements from a second GNSS constellation are used, instead of a single column with “1” for the clock offset in Equation 5, two columns with either “1” or “0” depending on the constellation per row would be added. This is done to select the specific constellation to which each of the satellites belongs to.

Additionally, the vertical ephemeris protection level ( $VPB$ ) is defined as:

$$VPB_i = |s_{vert,i}| \cdot x_{air} \cdot P_i + k_{md,e} \cdot \sqrt{\sum_{i=1}^N s_{vert,i}^2 \cdot \sigma_{GBAS,i}^2},$$

$$VPB = \max(VPB_i), \quad (7)$$

where  $x_{air}$  is the distance (in slant range) between the aircraft and the GBAS reference point (in meters),  $k_{md,e}$  represents the ephemeris missed detection multiplier of 3.8, and  $P_i$  represents the ephemeris decorrelation parameter for satellite  $i$  (set to 0.00018 according to [3]). These last two parameters are both dependent on the approach service type (see Section 2.3.11.5.2.4 of [14]). In this work, we use both  $VPL_{H0}$  and  $VPB$  since they are the most relevant when studying availability with respect to distance. Therefore, the  $VPL_{H1}$  is considered out of scope.

### III. IONOSPHERIC GRADIENT MONITORING CONCEPT

In this section, we describe the dual-frequency airborne ionospheric gradient monitor proposed for both the GAST F and GAST X architectures. Section III-A summarizes the ionospheric monitor presented previously in [9], Section III-B describes the derivation of both the constant and variable monitoring thresholds, Section III-C summarizes the adaptation of the monitor for a GAST X architecture presented in [10], and Section III-D describes the satellite exclusion and re-inclusion strategy together with the explanation of the switch to the I-free modes. This strategy will be used for both GAST F and GAST X architectures together with the thresholds proposed in this section to carry out the performance studies.

#### A. Test Statistic and Monitoring Condition

The ionospheric monitor concept presented in [9] proposes a method to compare a quantity derived from the transmitted pseudorange and range-rate corrections ( $\hat{I}_{PRC,i}$ ) to another quantity derived from ionospheric delay estimates in the airborne receiver ( $\hat{I}_{air,i}$ ). The  $\hat{I}_{PRC,i}$  for each satellite  $i$ , frequency L1, and the current epoch can be computed as:

$$\hat{I}_{PRC,i} = \frac{f_{L5}^2}{f_{L1}^2 - f_{L5}^2} \cdot [(PRC_{L5,i} + \Delta t \cdot RRC_{L5,i}) - (PRC_{L1,i} + \Delta t \cdot RRC_{L1,i})], \quad (8)$$

where  $PRC_i$  and  $RRC_i$  are the pseudorange and range-rate corrections on either L1/E1 or L5/E5a and  $\Delta t$  the time difference between the current time of airborne measurement and the time of generation of the corrections. Note that the  $\hat{I}_{PRC,i}$  values are considered “pseudo ionospheric delays” because the ionospheric delays experienced at the GBAS ground station cannot be directly recovered from the corrections received by the aircraft due to the smooth clock corrections and averaging steps carried out in the PRC generation process.

In the airborne system the ionosphere for satellite  $i$ , frequency L1, and the current epoch can be directly estimated using smoothed pseudoranges ( $\bar{\rho}$ ) on two frequencies:

$$\hat{I}_{air,i} = \frac{f_{L5}^2}{f_{L1}^2 - f_{L5}^2} \cdot (\bar{\rho}_{L5,air,i} - \bar{\rho}_{L1,air,i}). \quad (9)$$

While the absolute ionospheric delays seen by the GBAS ground station cannot be recovered from the corrections, the relative ionospheric differences between all satellites are still preserved within  $\hat{I}_{PRC,i}$ . Therefore, the test statistic designed for this monitor describes for each satellite how much an ionospheric estimate differs from the ionospheric pattern (i.e., the relative ionospheric delays among all the satellites) common to air and ground. The test statistic for satellite  $i$  and frequency L1 at the current epoch is thus calculated as:

$$I_{test,i} = \hat{I}_{air,i} + \hat{I}_{PRC,i} - \text{median}\{\{\hat{I}_{air,j} + \hat{I}_{PRC,j}\}_{j \in N}\} \quad (10)$$

where  $N$  refers to the set of common satellites for both air and ground per constellation. Note that since the monitoring is carried out in the position domain, the median-removal step in Equation 10 can be skipped because any biases that are common to all satellites will project into the clock estimate.

Once the test statistic is defined, the condition for detecting gradients can be presented. Note that ionospheric gradients are problematic when the position error they introduce is greater than a certain vertical error limit represented by  $E_{v,iono}$ , which is derived from operational requirements and explained in Section III-B. For this reason, the entire visible constellation of satellites is monitored first, so that if the satellite geometries are good enough that there may be some satellites with a low weight in the position solution affected and yet the position error is less than  $E_{v,iono}$ , no satellites will be discarded. The monitoring condition for the whole constellation is therefore:

$$VPL_{iono} = \left| \sum_{i=1}^N (I_{test,i} \cdot s_{vert,i}) \right| + k_{md,iono} \cdot \sqrt{\sum_{i=1}^N \sigma_{m,i}^2 \cdot s_{vert,i}^2} \leq E_{v,iono}, \quad (11)$$

where  $s_{vert,i}$  is the vertical projection factor onto the approach plane in the position solution and

$$\sigma_{m,i} = \frac{f_{L5}^2}{f_{L1}^2 - f_{L5}^2} \cdot \sqrt{\sigma_{gnd,L1}^2 + \sigma_{gnd,L5}^2 + \sigma_{air,L1}^2 + \sigma_{air,L5}^2} \quad (12)$$

describes the residual noise and multipath in the pseudorange corrections (the  $\sigma_{gnd}$ ) and the pseudorange measurements after

smoothing (the  $\sigma_{air}$ ) for each frequency. The  $k_{md,iono}$  factor results from the allocated integrity risk for the monitor (i.e. 6.1 for a probability of missed detection of  $10^{-9}$ ). Note that Equation 12 assumes no correlation between the errors on L1 and L5 frequencies and does not consider so far non-modelled effects such as errors due to antenna group delay variations from the ground or inter-frequency biases. This is considered as part of the future work.

The left part of Equation 11 is named  $VPL_{iono}$  because the monitoring condition can also be seen as a bound of the estimated differential ionospheric error in the position domain. However, instead of comparing this particular “protection level” against the VAL, it is compared against a threshold for the exclusion of satellite signals that could potentially be misleading. Note that, in case of using  $VPL_{iono}$  as a typical protection level and comparing it directly with VAL, exceeding it would automatically lead to a loss of availability. However, in the proposed methodology, the monitor first tries to find a subset of satellites with which the aircraft can continue to estimate its position using the primary modes and maintain availability and continuity.

### B. Monitoring Threshold

After defining the monitoring condition in Section III-A, it is necessary to set a gradient detection threshold that determines when it is unsafe to use the signals from a given satellite or set of satellites. In this paper, we revisit the threshold design and evaluate the performance of the monitor using two different thresholds: (i) a constant threshold derived from operational requirements, and (ii) a dynamic threshold that increases with distance to the airport.

#### Constant Monitoring Threshold

The value for the monitoring threshold used in Equation 11 ( $E_{v,iono}$ ) can be defined as the maximum error that an aircraft can tolerate due to an abnormal ionospheric gradient being present. Ideally, this value should be defined by aircraft manufacturers. However, up to date, there is no consensus from the aviation community on how large this value should be since it depends on the performance of the autopilot and navigation system installed in the aircraft (which may differ between different types of aircraft and aircraft manufactures).

As a solution to this problem, in [12], the authors propose to determine a constant threshold for the ionospheric gradient monitor based on the airworthiness requirements to support Category III operations [15]. In this work, we use the value derived for  $E_{v,iono}$  in [12] as the constant threshold for our monitor (i.e. it stays constant since the aircraft enters the Precision Approach Region (PAR) until it touches down). Therefore, the justifications behind the computation of  $E_{v,iono}$  are summarized here only briefly. For further details on the computation of  $E_{v,iono}$ , the reader is referred to [12].

There are three key conditions for which airworthiness requirements exist regarding performance: (i) nominal conditions, (ii) limit case condition, and (iii) malfunction condition. For a landing to be considered safe in nominal conditions,

the aircraft must land within the so-called “touchdown box”. Thus, the aircraft must touch down not less than 200 feet nor more than 2,700 feet behind the runway threshold, and not less than 5 feet from either runway edge with probability not less than  $1 - 10^{-6}$  ([16], [17]). In the limit case, performance must be demonstrated when one of the variables is at its “most critical value” while the other vary in their expected ranges. In the malfunction case, an undetected error occurs. In both limit and malfunction cases, the aircraft must also land within the touchdown box, where the land long limitation is extended 3000 feet behind the runway threshold. Considering the definitions of each case in [18], the anomalous ionosphere is typically considered within the malfunction case.

In the malfunction case, the aircraft must land within the touchdown box with probability 1. This requirement together with the constraint of the short landing case were considered in [12] to compute the along track error due to an additional undetected error in the form of a bias (e.g., caused by an anomalous ionospheric gradient) that adds to the nominal flight technical error (i.e., performance of the autopilot) and the nominal error of the navigation system (i.e., nominal errors due to noise, multipath decorrelation, nominal ionosphere and troposphere). The  $E_{v,iono}$  is computed by projecting the along track error into the vertical domain. Therefore, we calculate  $E_{v,iono}$  as:

$$E_{v,iono} = \tan(GPA) \cdot (NTDP - FTE_{ff,95\%} - 200) \cdot 0.3048 - NSE_{vert,ff,95\%}, \quad (13)$$

where  $NTDP = 1290$  feet is the Nominal Touch Down Point,  $FTE_{ff,95\%} = 1.96 \cdot \sigma_{FTE}$  is the 95th percentile of the Flight Technical Error,  $NSE_{vert,ff,95\%} = 1.96 \cdot (VPL/k_{ffmd})$  is the Navigation System Error computed from the VPL and the fault-free missed detection multiplier, and 0.3048 is the factor to transform feet into meters. These requirements are defined at aircraft level and therefore, in this work, typical values are assumed to compute  $E_{v,iono}$ . These values are:  $\sigma_{FTE} = 180$  feet,  $VPL = VAL = 10$  meters,  $k_{ffmd} = 5.81$ , and GPA of  $3^\circ$ . Consequently, the constant value for  $E_{v,iono}$  used in this work is 8.4 meters.

Note that it is likely that modern state-of-the-art autopilot systems have a better performance than that reflected in this paper by a  $\sigma_{FTE}$  of 180 feet, which would automatically increase the value of  $E_{v,iono}$ .

#### Variable Monitoring Threshold

The objective of this study is to assess whether increasing the threshold when the aircraft is at distances further away than the Decision Height (DH) distance is more beneficial than maintaining a constant value. Increasing the threshold allows more ionospheric error within the position solution further away from the airport, where larger errors may be less critical than when the aircraft is approaching touchdown. Therefore, it increases the likelihood of finding satellite subsets that would enable the use of the primary modes (either the GAST F based on single-frequency 100 seconds smoothing or the GAST X based on divergence-free 600 smoothing)

without the need to switch to the Ifree solution for a longer period. Note that, in general, the test statistic of the ionospheric monitor decreases as the ionospheric delay experienced by the ground station and an airborne user becomes more similar. A switch to the Ifree mode is generally considered irreversible for the remainder of the approach and, in general, worsens the performance because it combines the noise and multipath of two frequencies. Therefore, availability and continuity could be compromised in different cases (i.e., few satellites available due to maneuvers, etc.) if a constant threshold is used and switches to the Ifree mode occur more often than necessary.

Therefore, in this work, we propose to use a threshold that increases with the distance to the airport. Since the monitoring condition represented in Equation 11 is similar to that of a VPL, we have chosen the same function with which the VAL increases to increase  $E_{v,iono}$ . Table I represents the threshold as a function of the height of the aircraft ( $H_p$ ), which increases with the distance to the airport. In Table I,  $E_{v,DH}$  refers to the value of  $E_{v,iono}$  at the decision height.

TABLE I: Variable Monitoring Threshold

$E_{v,iono}$ (meters)	$H_p$ (meters)
$E_{v,DH}$	$H_p \leq 60.96$
$0.095965 \cdot H_p + E_{v,DH} - 5.85$	$60.96 < H_p \leq 408.432$
$E_{v,DH} + 33.35$	$H_p > 408.432$

As can be observed, the only change with respect to the VAL equation (Table 2-15 of [14]) is the value that  $E_{v,iono}$  takes at the decision height. Instead of the typical 10 metres of the VAL, we chose the 8.4 meters derived in the previous section to be consistent with the airworthiness operational requirements for Category III automatic landings. In case of relaxing some of the assumptions mentioned previously (e.g. lower flight technical errors), larger  $E_{v,iono}$  values at the decision height similar to those of the VAL, could be allowed.

### C. Adaptation of the Ionospheric Monitor for a GAST X Architecture

In the GAST X architecture, the raw measurements from each of the ground reference receivers are sent to the aircraft. Therefore, they can be used by the aircraft to compute the actual ground ionospheric delays for each satellite  $i$  and ground reference receiver  $k$  as explained in [10]:

$$\hat{I}_{gnd,k,i} = \frac{f_{L5}^2}{f_{L1}^2 - f_{L5}^2} \cdot (\bar{\rho}_{Dfree,L5,gnd,k,i} - \bar{\rho}_{Dfree,L1,gnd,k,i}). \quad (14)$$

The total ground ionospheric delay is computed as an average of the ionospheric delays from the  $M$  ground reference receivers as:

$$\hat{I}_{gnd,i} = \sum_{k=1}^M \hat{I}_{gnd,k,i}. \quad (15)$$

Therefore, in Equation 10, GAST X uses  $-\hat{I}_{gnd,i}$  instead of  $\hat{I}_{PRC,i}$ . The rest of the calculation of  $VPL_{iono}$  is analogous to that of the GAST F architecture in Equation 11 except

for the fact that  $\sigma_{m,i}$  (representing the nominal noise and multipath of  $I_{test,i}$ ) is lower due to the longer smoothing applied in GAST X. Note that,  $\hat{I}_{air,i}$  in Equation 9 for GAST X is calculated with  $\bar{\rho}_{Dfree,L5,air,i}$  and  $\bar{\rho}_{Dfree,L1,air,i}$  instead of SF 100-second smoothed pseudoranges as in GAST F. Furthermore,  $I_{test,i}$  in GAST X does not have the filter build-up error that the GAST F  $I_{test,i}$  experiences because GAST X utilizes divergence-free smoothing instead of single-frequency smoothing. More details of the differences between GAST F and GAST X can be found in [10].

### D. Satellite Exclusion and Switch to the Ifree Mode Strategy

In [9], we proposed a greedy exclusion algorithm to remove affected satellites. This algorithm checks if the monitoring threshold is exceeded taking into account all tracked dual-frequency satellites common to both ground and air. If the threshold is exceeded, then satellites are removed one by one, minimizing  $VPL_{iono}$ . When a subset is found that falls below the threshold, this subset is used in the current epoch. If no subset is found ( $N$  is below 5 satellites for the dual constellation (DC) case or below 4 for the single constellation (SC) case), a switch to the Ifree positioning mode is triggered and this mode is used for the remainder of the approach. This algorithm excludes the satellites for the remainder of the approach, i.e. if a satellite is excluded immediately after the aircraft enters the PAR (with the monitor switched on) it will remain unavailable until the aircraft touches down, even if the satellite is no longer affected by an ionospheric gradient during this period.

Excluding the satellites for the remainder of the approach instead of only during the period of time they are affected, increases the likelihood of switching to Ifree due to a lower number of satellites available. Therefore, we propose to exclude the satellites only one epoch and let the monitor select in every epoch which set of satellites provides an optimal performance. Since the smoothing filters are not re-started after a satellite is excluded, at every epoch, the monitor can compute the  $VPL_{iono}$  using all visible dual-frequency satellites again. Figure 1 shows the satellite exclusion and switching logic.

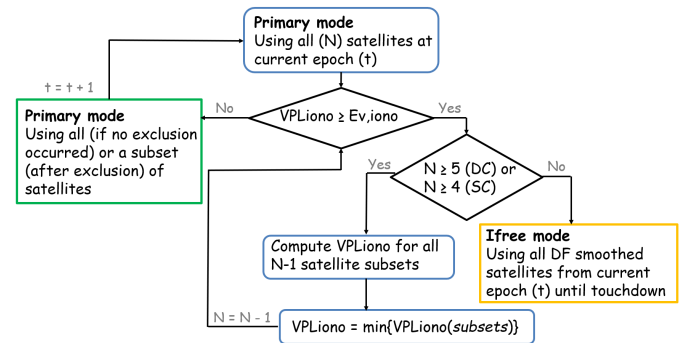


Fig. 1: Satellite exclusion and switching logic.

Furthermore, we propose to use the same satellite exclusion strategy in GAST X, as opposed to the concept proposed in [10], where after exceeding the threshold, a switch to the

Ifree mode is automatically triggered. Note that, typically, the monitor will discard always the same satellite(s) (i.e. the ones that are affected by an anomalous ionospheric gradient) and re-include them back when they are either slightly affected or unaffected, avoiding the use of a different subset of satellites each epoch.

#### IV. SIMULATION SETUP

In this section, we introduce the simulation setup that we used to evaluate the performance of the DF airborne ionospheric gradient monitor and the different DFMC processing modes. The simulation setup consists of 11 days of simulated satellite geometries using the orbital parameters from the so-called ‘‘Optimized 24 GPS Constellation’’ as defined in [19] and an ‘‘Optimized 24 Galileo Constellation’’ [20]. We simulated these satellite geometries for the three GBAS reference receivers installed at Tenerife Norte airport and a total of 78293 approaches following a regular approach trajectory towards the airport.

For each of the satellites, we simulated a nominal slant ionospheric delay based on the Klobuchar model [21] and an additional synthetic abnormal ionospheric delay based on real ionospheric perturbations. With the simulated ionospheric delay for each satellite observed by each ground reference receiver and the user and for each frequency (i.e., the ionospheric delay for L5/E5a is 1.8 times the simulated ionospheric delay for L1/E1), we calculated  $I_{test,i}$  as in Equation 10 for both GAST F (following Equations 8 and 9) and GAST X (following Equations 15 and 9). Then, we added representative noise and multipath for both GAST F and GAST X to  $I_{test,i}$ . In Section IV-A, we explain the process to simulate anomalous ionospheric gradients from real perturbations and in Section IV-B the process to add realistic noise and multipath to the test statistics.

The associated error models to compute  $\sigma_{GBAS,i}$  in Equation 2 and  $\sigma_{m,i}$  in Equation 12 for each processing mode can be found in Table II. All the cases in the table assume a GAD C [22] ground facility. We assumed the airborne receiver to be characterized by Airborne Accuracy Designator B (AAD B) [13] and we used the airborne multipath and antenna group delay variation models from [23]. Since both the ground and airborne noise and multipath models have been derived for SF 100-second smoothing, a scaling is necessary to use these models in GAST X. In [8], the authors justified the use of  $\sqrt{100/200} = 0.7071$  as the scaling factor for both the airborne and ground error contributions. The antenna errors, however, are not reduced by smoothing and thus, the scaling factor is not applied. Note that, a scaling factor corresponding to 200 seconds smoothing instead of 600 seconds smoothing, was proposed in [8] as previous studies indicated that smoothing intervals longer than 200 seconds do not reduce the variance of the noise. This scaling factor also assumes that the multipath and noise are not correlated, which is considered the worst case as, in reality, when measurements are correlated, the scaling factor is expected to be lower. The residual tropospheric uncertainty is represented by the residual uncertainty in the

tropospheric refractivity index ( $\sigma_r$ ), scale height ( $h_0$ ), height difference between the GBAS reference point (GRP) and the aircraft ( $\Delta h$ ), and satellite elevation angle ( $el$ ). In this study, we assume that  $\Delta h = H_p$ . The residual ionospheric delay is a function of the residual uncertainty in the vertical ionospheric delay ( $\sigma_{vig}$ ), which typically contains another term to take into account anomalous troposphere ( $\sigma_{anom,tropo}$ ), the vertical-to-slant obliquity factor ( $F_{pp}$ ), the geometrical distance between the GRP and the aircraft ( $x_{air}$ ) and the product of the smoothing time constant and aircraft speed ( $v_{air}$ ). Note that, the last term is only present for GAST F, as it represents the filter error build-up effect due to the single-frequency smoothing.

For this study, we implemented only the basic functionalities for both GAST F and GAST X. In both cases, only the airborne ionospheric monitor and cycle slip detectors are used. Furthermore, in the case of GAST X, we assumed 600-second Dfree-smoothing and a scaling factor corresponding to 200 seconds smoothing instead of using variable smoothing time constants. Note that the Ifree backup modes for GAST F and GAST X are also different. Ifree for GAST F uses SF 100-seconds smoothed pseudoranges while Ifree for GAST X uses Dfree 600-seconds smoothed pseudoranges.

##### A. Synthetic Ionospheric Gradients

We designed the synthetic ionospheric gradients to be representative of real ionospheric perturbations. As real perturbations, we selected several Equatorial Plasma Bubbles (EPBs) affecting satellite G24 (from the GPS constellation) that occurred on the 28th of February 2015 in Bahir Dar, Ethiopia (see Figure 6 of [24]). Since Tenerife is also considered a low latitude region, we considered the perturbation in Ethiopia as a ‘‘worst-case’’ example for Tenerife. The shape and magnitude of the perturbation in [24] can be represented by the following equation in Total Electron Content Units (TECUs):

$$I_{anomalous,i} = \sum_{j=1}^J a_j \cdot e^{-\frac{(x_{iono,i}-b_j)^2}{c_j^2}}, \quad (16)$$

where  $x_{iono,i}$  is the coordinate of the Ionospheric Pierce Point or IPP (i.e. the intersection of the line of sight satellite-receiver with the ionosphere modelled as a ‘‘thin shell’’ located at a 350 km above the Earth’s surface [21]) for satellite  $i$  in the perturbation reference plane, being the horizontal axis aligned with the direction of propagation of the perturbation. The parameters  $a_j$ ,  $b_j$ , and  $c_j$  are defined as in Table III.

Figure 2 shows the simulated EPB sequence (colourful region around  $-16^\circ$  of longitude) between the dark red areas, which are the areas where the ionospheric delay values are nominal and only the simulated ionospheric delay from the Klobuchar model is present. The synthetic perturbation is only defined in the direction of propagation and therefore, in the direction perpendicular to it (i.e.,  $y_{iono,i}$ ),  $I_{anomalous,i}$  takes the same value as for  $y_{iono,i} = 0$ . More details on the process to translate IPP coordinates in latitude and longitude to the perturbation plane can be found in Appendix A of [25].

TABLE II: Error models

	GAST F SF	GAST F Ifree	GAST X Dfree	GAST X Ifree
Smoothing constant ( $\tau$ )	100 s		600 s	
$\sigma_{gnd}$	GAD-C (for 3 ground receivers)	2.58 · GAD-C (for 3 ground receivers)	0.7071 · GAD-C (for 3 ground receivers)	2.58 · 0.7071 · GAD-C (for 3 ground receivers)
$\sigma_{MP}$	L1: $0.11 + 0.03 \cdot \exp(-el/80)$ L5: $0.07 + 0.06 \cdot \exp(-el/50)$	$0.26 + 0.08 \cdot \exp(-el/80)$	L1: $0.7071 \cdot (0.11 + 0.03 \cdot \exp(-el/80))$ L5: $0.7071 \cdot (0.07 + 0.06 \cdot \exp(-el/50))$	$0.7071 \cdot (0.26 + 0.08 \cdot \exp(-el/80))$
$\sigma_{AGDV}$	$0.065 + 0.2 \cdot \exp(-el/14)$	$0.17 + 0.5 \cdot \exp(-el/15)$	$0.065 + 0.2 \cdot \exp(-el/14)$	$0.17 + 0.5 \cdot \exp(-el/15)$
$\sigma_n$	AAD-B	2.58 · AAD-B	0.7071 · AAD-B	2.58 · 0.7071 · AAD-B
$\sigma_{air}$	$\sqrt{\sigma_{MP}^2 + \sigma_{AGDV}^2 + \sigma_n^2}$			
$\sigma_{tropo}$	$\sigma_r \cdot h_0 \cdot \frac{10^{-6}}{\sqrt{0.002 + \sin^2(el)}} \cdot (1 - \exp(-\Delta h/h_0))$ with $\sigma_r = 40$ and $h_0 = 9$ km			
$\sigma_{vig}$	4 mm/km	0	4 mm/km	0
$\sigma_{anom,tropo}$	5 mm/km			
$\sigma_{iono}$	$F_{pp} \cdot \sqrt{\sigma_{vig}^2 + \sigma_{anom,tropo}^2} \cdot (x_{air} + 2 \cdot \tau \cdot v_{air})$		$F_{pp} \cdot \sqrt{\sigma_{vig}^2 + \sigma_{anom,tropo}^2} \cdot (x_{air})$	

TABLE III: Parameters for modelling an EPB sequence.

j	$a_j$	$b_i$	$c_i$
1	-3.530294	44.205242	7.882559
2	-6.482070	75.286176	11.915798
3	-7.871373	59.664475	6.288312
4	-1.896577	84.803193	1.457045
5	-3.734088	97.192591	6.264391
6	-2.921926	114.896822	11.886672

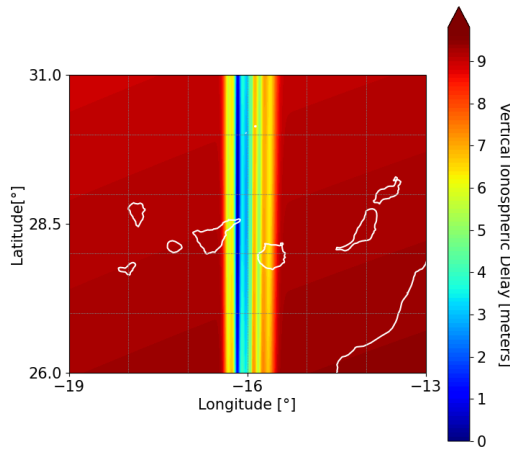


Fig. 2: Simulated EPB sequence (vertical ionospheric delay in meters of L1) affecting Tenerife Norte airport.

To obtain representative “worst-case results”, we assumed that the ionospheric delay represented in TECUs in [24] is already the ionospheric delay in metres of L1. Note that, 1 TECU corresponds to 0.162 metres of L1, which would make the simulated EPBs significantly smaller. We also assumed that the model is in the vertical domain and not in the slant domain like the real perturbation, since the case study in [24] was for a single satellite but we need to simulate the gradient for all satellites. Simulating the gradients first in the vertical domain allows them to be independent of the elevation of each of the satellites, which allows us to simulate

the same ionospheric gradient for all satellites. Therefore, when an IPP corresponding to a given satellite and ground reference receiver or user moved into the region with the gradient, we calculated the vertical ionospheric delay for that IPP and multiplied it by an obliquity factor (see equation 5.28 in [26]) that depends on the elevation of the satellite to obtain the slant delay. In addition, this ionospheric gradient moved with a constant velocity (100 m/s) and in an eastward direction. Note that, this is one example of a “worst-case” EPB sequence and more simulations with different EPBs or EPB threat models (i.e., different magnitudes, shapes, speeds, and directions) should be carried out to obtain more representative performance results.

### B. Addition of Time Correlated Noise and Multipath

For generating the satellite and mode specific noise values on the test statistic, we used a slightly modified autoregressive model of first order [27]. The general formulation of an  $AR(1)$  process is as follows:

$$X_t = \phi_1 \cdot X_{t-1} + \epsilon_t. \quad (17)$$

Here,  $\phi_1$  denotes the first (and in our case only) autoregression coefficient, and  $X_t$  denotes the process state at time  $t$ . Instead of a constant white noise process, we included an elevation dependency in the noise component  $\epsilon_t$ . The standard deviation of the samples of  $\epsilon_t$  is given in Equation 18.

$$\sigma_{\epsilon_{t,i}} = \sigma_{\epsilon 0} \cdot (1 + 3 \cdot e^{-el_{t,i}/30}) \quad (18)$$

The instantaneous noise added to the output in each epoch was therefore dependent on the current elevation ( $el_{t,i}$ ) of each satellite. In this way, we could reproduce the elevation dependency of  $I_{test,i}$  due to noise and multipath. Finally, another white noise term was added to get the final satellite specific noise process result in each epoch:

$$\begin{aligned} \tilde{X}_{t,i} &= X_{t,i} + \nu \\ \nu &\sim \mathcal{N}(0, \sigma_0). \end{aligned} \quad (19)$$

Table IV shows the parameters we used for the simulations. Those were estimated based on a sample of 24 hours of static data collected with a MLA (Multipath Limiting Antenna) installation at Tenerife Norte airport in combination with a close-by static user receiver. For a nominal day, we computed  $I_{test}$  for the different modes of interest and modelled the noise processes to achieve similar statistics and time behavior. In Figure 3 we compare the standard deviation (in elevation bins of 5 degrees) of the measurement data with 10 different noise realizations.

TABLE IV: Parameters used to model AR noise processed for the different simulated processing modes.

Mode	$\phi_1$	$\sigma_{\epsilon 0}$	$\sigma_0$
GAST F	0.99990	0.0021	0.00050
GAST X	0.99999	0.0009	0.00190

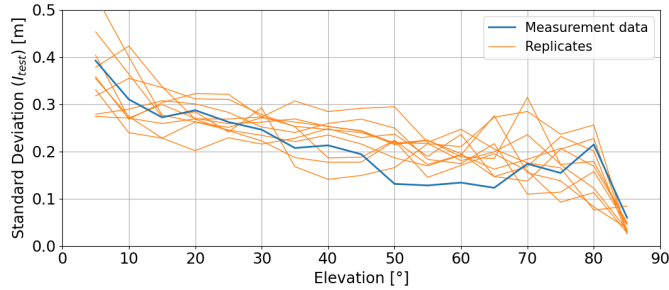


Fig. 3: Comparison of standard deviation of  $I_{test}$  (GAST F) for 24 h of measurements as well as 10 different replicates. The data is split into elevation bins of 5°.

The resulting noise terms were added to the synthetic, noise-free test statistic (Equation 20) as it was described in Section IV-A before applying the ionospheric monitoring.

$$\tilde{I}_{test,i} = I_{test,i} + \tilde{X}_{t,i} \quad (20)$$

## V. EXPERIMENTAL SETUP

Additionally to the previously described simulation setup, we also evaluated the performance of the DF airborne ionospheric gradient monitor and the different DFMC processing modes with real data. For the ground station, we used data from the three MLAs installed at Tenerife Norte airport (represented in black as RX1, RX2, and RX3 in Figure 4). As a user, we collected measurements on the 17th of November 2022. The experimental setup was a Tallysman TW7972 triple-band GNSS antenna installed on the roof of a car and a geodetic Javad Omega multi-frequency multi-constellation GNSS receiver. To be able to validate the variable threshold, we stopped at different distances from the airport, shown as points 1, 2 and 3 in Figure 4. At point 1 (located at 2.11 km from RX1), we collected measurements from 22:20 to 22:37 local time, at point 2 (located at 7.54 km), we collected measurements from 23:00 to 23:35 local time, and at point 3 (located at 10 km), we collected measurements from 23:45 to 00:26 local time.

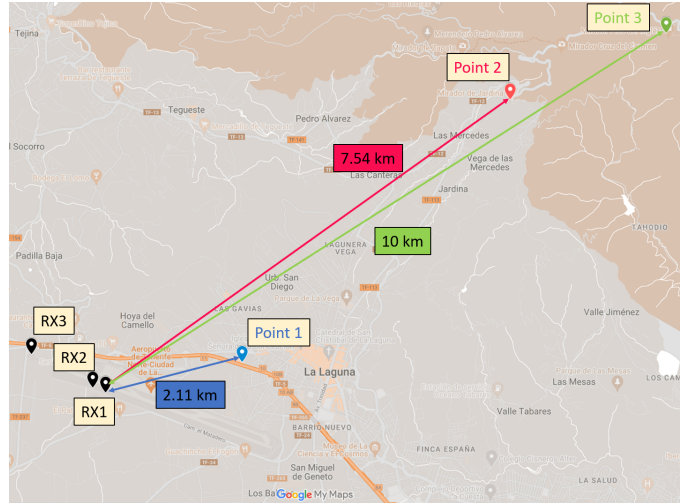


Fig. 4: Ground reference antennas (in black) and user locations (in blue, red, and green) where the real measurements were collected.

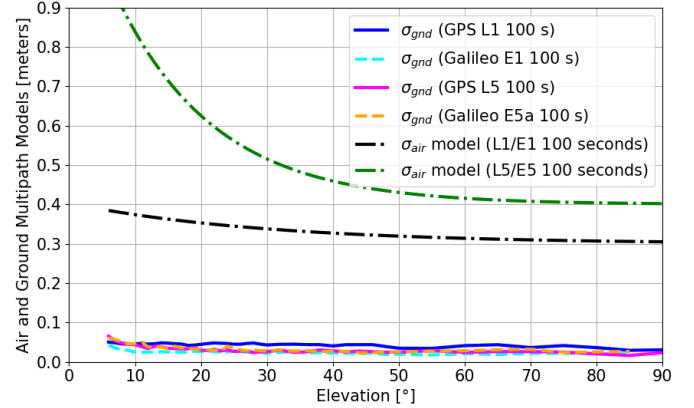


Fig. 5:  $\sigma_{gnd}$  and  $\sigma_{air}$  curves as a function of satellite elevation for Tenerife Norte airport and the user respectively.

Figure 5 shows the noise and multipath error models for both the ground station and the user. We computed the ground noise and multipath errors ( $\sigma_{gnd}$ ) using 24 hours of real measurements collected on a nominal day (i.e. no anomalous ionospheric gradients present). As can be observed, the ground noise and multipath levels are low, as expected from a real GBAS installation. On the contrary, the noise and multipath errors derived with 24 hours of real data in nominal conditions collected by the antenna installed in the rooftop of the car are high. Due to the numerous peaks produced by the multipath on the ground and the different obstacles, we derived a conservative model of the  $\sigma_{air}$  values from the measurements (black and green curves in Figure 5). Nevertheless, even without the peaks,  $\sigma_{air}$  is still significantly higher than the expected values of  $\sigma_{air}$  derived from a real installation in the aircraft [23]. The other error models (i.e. troposphere and ionosphere) are as the ones presented in Table II for the simulation part.

## VI. RESULTS AND DISCUSSION

### A. Evaluation of the Number of Switches to the I<sub>free</sub> Mode with Simulated Gradient Scenarios

From the total number of 78293 simulated approaches, 46441 were “active” (i.e., with an anomalous ionospheric gradient affecting one or several satellites observed by air, ground or both) and 31852 approaches were “non-active” (i.e., no anomalous ionospheric gradient is present and  $I_{test,i}$  from Equation 10 is mainly nominal ionosphere, noise and multipath).

Figure 6 shows the percentage of exclusions of one or more satellites and switches to the I<sub>free</sub> mode with respect to the number of approaches on active conditions and non-active conditions. In non-active conditions and dual-constellation scenarios, the monitor did not trigger any switches to I<sub>free</sub> nor did it exclude any satellites for GAST F and GAST X. However, in non-active conditions and single-constellation scenarios, both exclusions (light blue bars in Figure 6) and switches (orange bars in Figure 6) due to false alerts from the monitor can be seen. In these cases, the percentage of exclusions with respect to the approaches in non-active conditions (1.55% with a variable threshold and 1.58% with a constant threshold in GAST F and 0.53% with a variable threshold and 0.56% with a constant threshold in GAST X) was practically the same as that of switches with respect to the approaches in non-active conditions (1.54% with a variable threshold and 1.57% with a constant threshold in GAST F and 0.46% with a variable threshold and 0.49% with a constant threshold in GAST X). This is due to the fact that, in both cases, the satellite geometries were “weak” (with an average of 6 satellites in view and  $s_{vert,i}$  reaching values above 2.5) and therefore excluding satellites made the situation worse and led to a switch in most cases. Note that, in this case, the use of a variable threshold did not improve the switching rate for either GAST F or GAST X, although GAST X performed better due to its lower noise and multipath levels.

In active conditions and dual-constellation scenarios, the monitor did not trigger a switch to I<sub>free</sub> for GAST X using either the constant or variable thresholds, which means that it was possible for the ionospheric monitor to find a subset of satellites that would still have enough performance in the primary mode. Here, an improvement can be seen when the monitor used the variable threshold to when the monitor used the constant threshold. There were 0% exclusions with respect to the number of approaches in active conditions with the variable threshold, while there were 0.14% exclusions with the constant threshold. In the case of GAST F, there were only few switches (0.002% and 0.013% with the variable and constant thresholds respectively) and exclusions (0.065% and 2.13% with the variable and constant thresholds respectively). Here, the use of a variable threshold reduced the exclusion and switching rates for both GAST F and GAST X. Furthermore, the difference in performance is clearer, as GAST X also has the advantage of not having the single-frequency filter build-up error in active conditions. These differences between

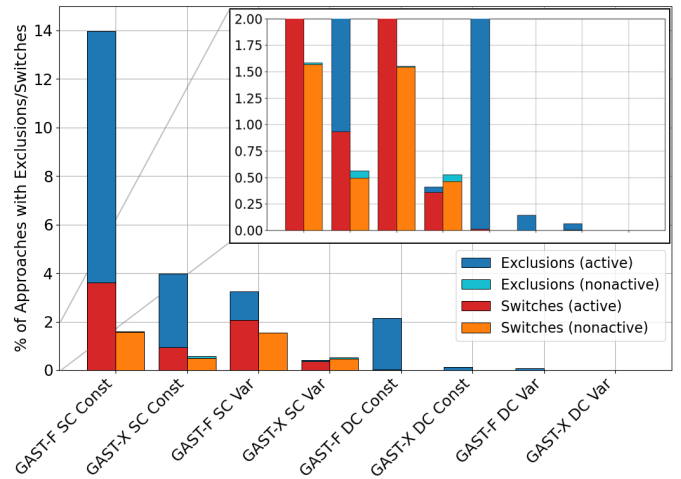


Fig. 6: Overview of the number of approaches with exclusions and switches for all studied processing modes. For each mode, the left bar shows the result for active conditions, while the right bar shows the nominal cases.

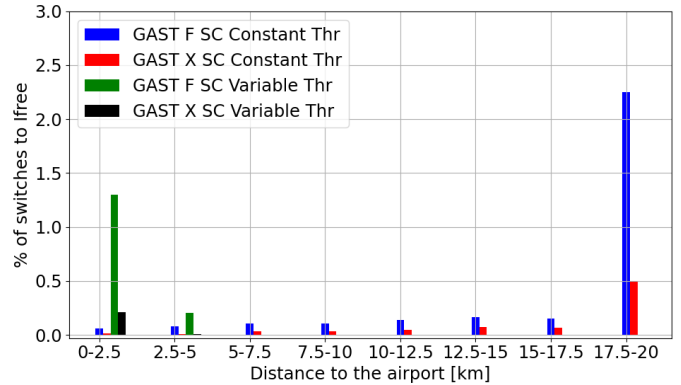


Fig. 7: Percentage of switches from the primary modes (SF in GAST F and D<sub>free</sub> in GAST X) to their corresponding I<sub>free</sub> mode in single constellation scenarios and active ionospheric conditions with respect to the aircraft distance from the airport.

the number of exclusions and switches between GAST F and GAST X and the use of the two thresholds (i.e. variable and constant) were more evident in the case of single constellation scenarios. When using a variable threshold, the number of switches (0.36%) was very similar to the number of exclusions in GAST X (0.41%). This was again due to the “weak” geometries mentioned in the non-active cases, which meant that at the moment the affected satellite was discarded (typically only 1 affected satellite for a 6-satellite geometry or 2 affected satellites for an 8-satellite geometry), the primary mode did not have sufficient performance and a switch to I<sub>free</sub> was triggered. The use of a constant threshold in GAST X SC caused more satellites to be discarded (3.99%) and also more switches (0.93%). The same is observable in GAST F, with a significant number of exclusions in the case of using a constant threshold (a 13.98% with the constant

threshold versus a 3.25% with the variable threshold) and a still low number of switches, especially when using the variable threshold (a 2.05% with the variable threshold and a 3.61% with the constant threshold). For both GAST X and GAST F, exclusions typically occurred when the satellite or the two satellites with the highest  $s_{vert,i}$  were affected.

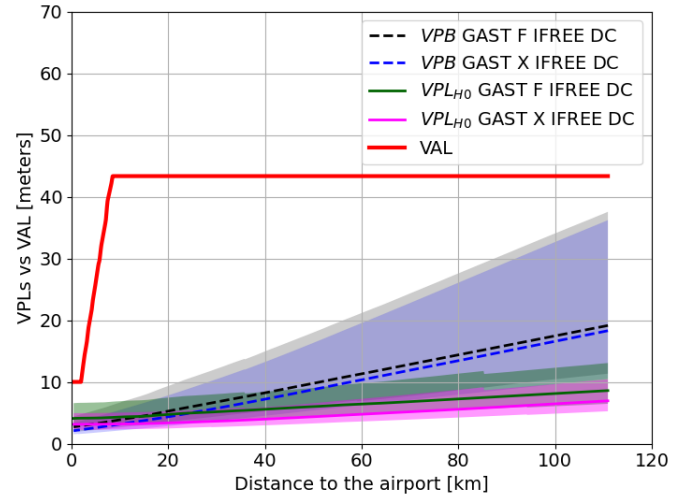
Figure 7 shows the percentage of switches from the primary modes to Ifree in single constellation scenarios and active conditions with respect to the user distances from the airport. For both GAST F and GAST X, when using a variable threshold, the majority of switches occurred at the end of the trajectory of the simulated aircraft. In these cases, the aircraft was already within or close to the DH distance and the variable threshold approached the value of the constant threshold. When the constant threshold was used, the switches occurred at different distances from the airport with a predominance when the aircraft entered the PAR and the monitor was switched on. This is because, in this case, the threshold was at its most stringent value throughout all distances from the airport. Note that the percentages calculated in Figures 6 and 7 are computed with respect to a different number of approaches (46441 for active and 31852 non-active).

From the results above, we can conclude that the GAST X mode has a slightly better performance in terms of switching to Ifree in dual-constellation scenarios, although the performance for the GAST F mode is also satisfactory. In single-constellation scenarios, the GAST X mode has also a better performance than GAST F, although both modes need to switch to Ifree when weak geometries together with 1 or more satellites heavily affected are combined. Furthermore, using a variable threshold helps to reduce the number of switches to the Ifree mode for single-constellation scenarios, especially in active conditions, since almost half of the switches are avoided. Note that these studies have been carried out using the baseline number of satellites for both GPS (24 satellites) and Galileo (24 satellites) and therefore the results using the typical recent number of operational GPS satellites and planned Galileo satellites (both around 30) are expected to be better.

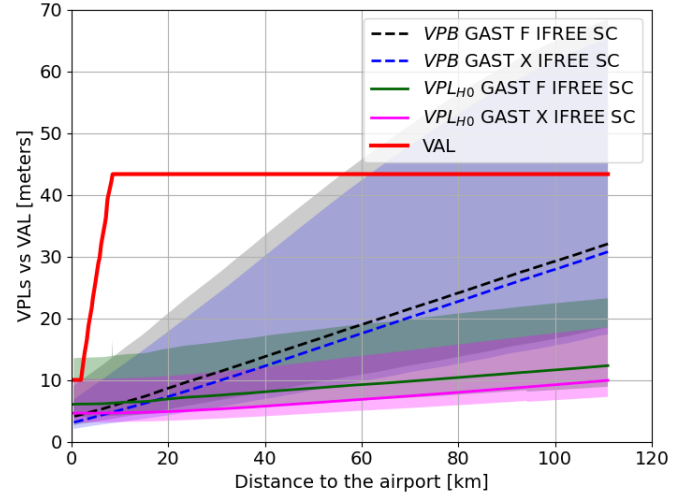
#### B. Availability of the Ifree mode for both GAST F and GAST X with Simulated Gradient Scenarios

The trigger of a switch to the Ifree mode by the monitor in GAST F or GAST X does not lead to an automatic loss of availability or continuity. In most cases, even with an increased level of noise and multipath in its position estimation, the aircraft will still be able to land safely by using the Ifree mode. In this section, we compare the Ifree  $VPL_{H0}$  and the  $VPB$  with the VAL and calculate the availability for the different modes under study and all the approaches (i.e. active and non-active) introduced in the previous section.

Figure 8a shows the mean, maximum, and minimum values of the nominal and ephemeris vertical protection levels calculated for all the simulated approaches and dual-constellation scenarios. Below 13.5 km for GAST F and 10.6 km for GAST X, the  $VPL_{H0}$  was the predominant value, while



(a) Dual-constellation scenarios.



(b) Single-constellation scenarios.

Fig. 8: Dual-constellation (a) and single-constellation (b) Ifree vertical protection levels for both GAST X and GAST F with respect to the distance from the airport. The lines (dashed for the  $VPB$  and continuous for  $VPL_{H0}$ ) show the mean values while the filled areas represent the space between the maximum and minimum values of the corresponding protection level represented by each color.

further away from the airport,  $VPB$  was higher. In this case, in the event of switching to Ifree, an availability of 100% (of the simulated cases) would be achieved for both GAST F and GAST X.

Figure 8b shows the mean, maximum, and minimum values of the nominal and ephemeris vertical protection levels calculated for all the simulated approaches and single-constellation scenarios. The  $VPL_{H0}$  was the predominant value below 10 km for GAST F and 8 km for GAST X, while at further away distances from the airport,  $VPB$  was higher. However, the maximum values for  $VPL_{H0}$  exceeded the values of VAL at close distances from the airport and an availability of 100%

was not achieved. In this case, the availability considering all approaches was 99.95% (of the simulated cases) for GAST F and 99.96% (of the simulated cases) for GAST X.

### C. Results with Real Measurements

In this section, we present the results obtained using the data from the experimental setup described in Section V.

Figure 9 shows the slant ionospheric delay (in meters of L1) calculated with the carrier-phase measurements at frequencies L1/E1 and L5/E5a collected by the receiver installed in the car. Note that Figure 9 only shows the delays computed at the times when the car was static, since the data when the car was moving were unusable due to cycle slips and regular signal losses due to obstructions. During the periods studied, some small-scale ionospheric disturbances occurred. There was also scintillation, which did not allow the smoothing filters to converge for some of the satellites, thus losing them. Due to the limited amount of data collected, only 200-seconds smoothing could be applied to GAST X (as opposed to the usual 600 seconds).

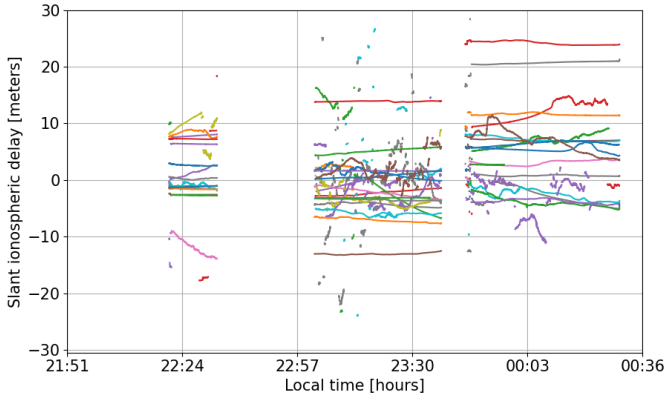


Fig. 9: Slant ionospheric delay (in meters of L1) calculated with the carrier-phase measurements on L1/E1 and L5/E5a frequencies collected by the receiver installed in the car.

Figure 10 shows the  $VPL_{iono}$  and threshold computed for both GAST F and GAST X. Note that the exclusion of satellites has been deactivated in order to observe the values that  $VPL_{iono}$  reaches. The variable threshold managed to avoid triggering the monitor threshold in points 2 and 3. When the variable threshold was at its most stringent value (in the results of point 1), both GAST F and GAST X exceeded the threshold. However it should be noted that this high  $VPL_{iono}$  values were due to “weak” satellite geometries together with a large  $\sigma_{air}$ , which made GAST X slightly better than GAST F, but the monitor still triggered a switch to Ifree for both modes in point 1.

Figure 11 shows the Ifree  $VPL_{H0}$  and  $VPB$  calculated for both GAST F and GAST X. In both Ifree modes, availability and continuity were maintained for points 2 and 3. At point 1, both GAST F and GAST X were unavailable due to the high  $\sigma_{air}$  values, especially for GAST F, and to not having enough smoothed satellite measurements available in GAST X. The

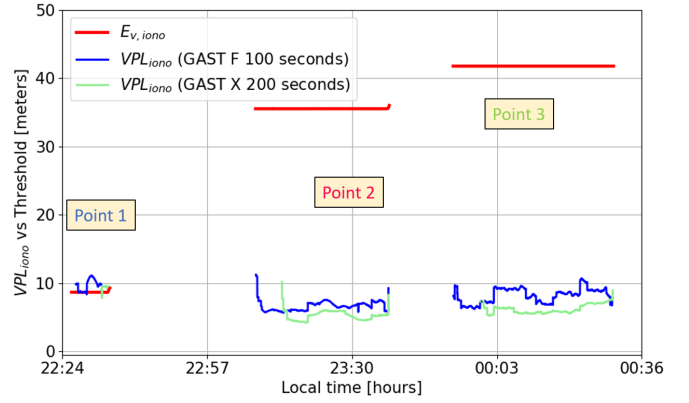


Fig. 10:  $VPL_{iono}$  and threshold computed for both GAST F and GAST X and the different distances from the airport where data were collected.

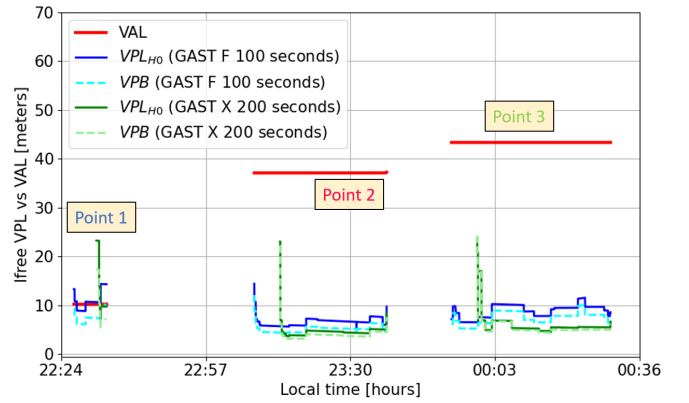


Fig. 11: Ifree nominal and ephemeris vertical protection levels computed for both GAST F and GAST X and the different distances from the airport where data were collected.

reason behind is that in GAST X the smoothing filters took double the time to converge (12 minutes instead of 6 minutes).

## VII. CONCLUSIONS AND FUTURE WORK

In this paper, we proposed the use of a variable threshold for the dual-frequency airborne ionospheric gradient monitor developed for DFMC GBAS. The results, both with simulated and real data, showed that the variable threshold significantly reduces the probability of excluding satellites (both in cases where satellites are affected and due to false alerts) and of switching to Ifree modes for both dual-constellation and single-constellation scenarios. This is important as, in case the two constellations transmitted by the ground station and the two constellations tracked by the aircraft are not the same, the single-constellation scenarios might be more likely than initially expected for DFMC GBAS. Furthermore, we evaluated the availability of GAST F and GAST X Ifree modes with simulated and real data. In the case of simulated data, the availability of the Ifree modes was 100% for GAST F/X DC and very similar for SC (99.95% and 99.96% respectively).

For the real data, both modes were unavailable at a close distance to the airport due to the high  $\sigma_{air}$  used. In general, the GAST X mode was more robust to satellite exclusions and switching to Ifree, especially in single constellation, due to its lower noise and multipath levels as well as not having the filter build-up errors. However, both modes had sufficient performance in the dual-constellation scenarios studied in this work. This means that, if a way can be found to ensure that two constellations are common between ground and air, either architecture (i.e. GAST F or GAST X) could be selected as the primary mode for future DFMC GBAS.

Future work will focus on validating the ionospheric monitor with real data in active conditions collected by installations with a performance similar to an aircraft. It will also address other effects, such as errors due to elevation and azimuth-dependent ground antenna delay variations. Furthermore, the impact of inter-frequency biases on the Ifree modes will be assessed.

#### ACKNOWLEDGMENT

The authors would like to thank Enaire, INDRA Satnav, and INDRA Navia for providing the data from the GBAS installation in Tenerife in the frame of the European project SESAR 2020 PJ14 W2 WP9 Sol79b.

#### REFERENCES

- [1] S. Pullen, Y. S. Park, and P. Enge, "Impact and mitigation of ionospheric anomalies on ground-based augmentation of GNSS," *Radio Science*, vol. 44, 2009.
- [2] J. Lee, J. Seo, Y. Park, S. Pullen, and P. Enge, "Ionospheric Threat Mitigation by Geometry Screening in Ground-Based Augmentation Systems," *Journal of Aircraft*, vol. 48, no. 4, pp. 1422–1433, 2011.
- [3] M. Yoon, D. Kim, S. Pullen, and J. Lee, "Assessment and mitigation of equatorial plasma bubble impacts on category I GBAS operations in the Brazilian region," *Navigation*, vol. 66, no. 3, pp. 643–659, 2019.
- [4] S. Pullen, R. Cassell, B. Johnson, *et al.*, "Impact of Ionospheric Anomalies on GBAS GAST D Service and Validation of Relevant ICAO SARPs Requirements," *Proceedings of the 30th International Technical Meeting of the Satellite Division of The Institute of Navigation (ION GNSS+ 2017)*, pp. 2085–2105, 2017.
- [5] M. Yoon, J. Lee, and S. Pullen, "Integrity risk evaluation of impact of ionospheric anomalies on GAST D GBAS," *NAVIGATION*, vol. 67, no. 2, pp. 223–234, 2020.
- [6] ICAO, "ICAO Working Paper: NSP 5 WP 41 – DFMC GBAS Conceptual Framework – SESAR Joint Undertaking," Tech. Rep., 2018.
- [7] T. Murphy, M. Harris, G. McGraw, *et al.*, "Alternative Architecture for Dual Frequency Multi-Constellation GBAS," in *Proceedings of the 34th International Technical Meeting of the Satellite Division of The Institute of Navigation (ION GNSS+ 2021)*, 2021, pp. 1334–1374.
- [8] T. Murphy, M. Harris, G. Balvedi, *et al.*, "Availability of Iono Gradient Detection with Alternative Architectures for DFMC GBAS," in *Proceedings of the 35th International Technical Meeting of the Satellite Division of The Institute of Navigation (ION GNSS+ 2022)*, 2022, pp. 12–33.
- [9] D. Gerbeth, M. Caamano, M.-S. Ciriuciu, and M. Felux, "Airborne Ionospheric Gradient Monitoring for Dual-Frequency GBAS," in *Proceedings of the 2022 International Technical Meeting of The Institute of Navigation*, 2022, pp. 1110–1122.
- [10] T. Murphy, M. Harris, G. Balvedi, *et al.*, "Ionospheric Gradient Monitoring for Dual Frequency Multi-Constellation GBAS," in *Proceedings of the 2022 International Technical Meeting of The Institute of Navigation*, 2022, pp. 1075–1097.
- [11] S. Saito, T. Yoshihara, T. Murphy, *et al.*, "Validation of Ionospheric Anomaly Monitor for DFMC GBAS under Disturbed Ionospheric Conditions," in *Proceedings of the 35th International Technical Meeting of the Satellite Division of The Institute of Navigation (ION GNSS+ 2022)*, 2022, pp. 3150–3159.
- [12] M. Felux, M.-S. Ciriuciu, J. Lee, and F. Holzapfel, "Ionospheric Gradient Threat Mitigation in Future Dual Frequency GBAS," *International Journal of Aerospace Engineering*, 2017.
- [13] International Civil Aviation Organization, "International Standards and Recommended Practices (SARPs). Annex 10 to the Convention of International Civil Aviation. Volume I -Radio Navigation Aids," Tech. Rep., 2017.
- [14] Radio Technical Commission for Aeronautics, "DO-253D, Minimum Operational Performance Standards for GPS Local Area Augmentation System Airborne Equipment," Tech. Rep., 2017.
- [15] W. Schuster and W. Ochieng, "Harmonisation of category-III precision approach navigation system performance requirements," *The Journal of Navigation*, vol. 63, no. 4, p. 569, 2010.
- [16] FAA, "Circular 120-28D: Criteria for approval of category III weather minima for takeoff, landing and rollout," Tech. Rep., 1999.
- [17] J. Wanner, "Certification Specifications for All Weather Operation, CS-AWO," *European Aviation Safety Agency EASA Brussels*, 2003.
- [18] T. Murphy, M. Harris, C. Shively, L. Azoulai, and M. Brenner, "Fault modeling for GBAS airworthiness assessments," *Navigation: Journal of The Institute of Navigation*, vol. 59, no. 2, pp. 145–161, 2012.
- [19] U.S. Dept. of Defense, "Global Positioning System Standard Positioning Service Performance Standard, 4th Edition," Sep. 2008.
- [20] *Galileo Open Service - Service Definition Document (OS SDD v1.2)*, Nov. 2021.
- [21] J. Klobuchar, "Ionospheric Time-Delay Algorithm for Single-Frequency GPS Users," *IEEE Transactions on aerospace and electronic systems*, no. 3, pp. 325–331, 1987.
- [22] G. A. McGraw, T. Murphy, M. Brenner, S. Pullen, and A. J. V. Dierendonck, "Development of the LAAS Accuracy Models," in *Proceedings of the 13th International Technical Meeting of the Satellite Division of The Institute of Navigation (ION GPS 2000)*, Sep. 2000, pp. 1212–1223.
- [23] M.-S. Ciriuciu, S. Caizzzone, C. Enneking, *et al.*, "Final Results on Airborne Multipath Models for Dualconstellation Dual-frequency Aviation Applications," in *Proceedings of the 2021 International Technical Meeting of The Institute of Navigation*, 2021, pp. 714–727.
- [24] M. Kriegel, N. Jakowski, J. Berdermann, H. Sato, and M. W. Mersha, "Scintillation measurements at Bahir Dar during the high solar activity phase of solar cycle 24," in *Annales Geophysicae*, vol. 35, 2017, pp. 97–106.
- [25] M. Caamaño Albuerno, "Network-based Ionospheric Gradient Monitoring to Support Ground Based Augmentation Systems," *Dissertation, Universitat Politècnica de Catalunya*, 2022.
- [26] P. Misra and P. Enge, *Global Positioning System: Signals, Measurements and Performance Second Edition*. Massachusetts: Ganga-Jamuna Press, 2006.
- [27] G. E. P. Box, G. M. Jenkins, G. C. Reinsel, and G. M. Ljung, *Time Series Analysis - Forecasting and Control*. New York: John Wiley & Sons, 2015.